European Journal of Nuclear Medicine and Molecular Imaging (2019) 46:1940–1951
https://doi.org/10.1007/s00259-019-04347-y

ORIGINAL ARTICLE

PET imaging of distinct brain uptake of a nanobody and similarly-sized PAMAM dendrimers after intra-arterial administration

Wojciech G. Lesniak[1] · Chengyan Chu[1,2] · Anna Jablonska[1,2] · Babak Behnam Azad[1] · Olivier Zwaenepoel[3] · Michal Zawadzki[4] · Ala Lisok[1] · Martin G. Pomper[1] · Piotr Walczak[1,2] · Jan Gettemans[3] · Miroslaw Janowski[1,2]

Received: 2 December 2018 / Accepted: 29 April 2019 / Published online: 3 June 2019

Abstract

Introduction We have recently shown that intracerebral delivery of an anti-VEGF monoclonal antibody bevacizumab using an intra-arterial (IA) infusion is more effective than intravenous administration. While antibodies are quickly emerging as therapeutics, their disadvantages such as large size, production logistics and immunogenicity motivate search for alternatives. Thus we have studied brain uptake of nanobodies and polyamidoamine (PAMAM) dendrimers.

Methods Nanobodies were conjugated with deferoxamine (DFO) to generate $NB(DFO)_2$. Generation-4 PAMAM dendrimers were conjugated with DFO, and subsequently primary amines were capped with butane-1,2-diol functionalities to generate $G4(DFO)_3(Bdiol)_{110}$. Resulting conjugates were radiolabeled with zirconium-89. Brain uptake of $^{89}ZrNB(DFO)_2$ and $^{89}ZrG4(DFO)_3(Bdiol)_{110}$ upon carotid artery vs tail vein infusions with intact BBB or osmotic blood–brain barrier opening (OBBBO) with mannitol in mice was monitored by dynamic positron emission tomography (PET) over 30 min to assess brain uptake and clearance, followed by whole-body PET-CT (computed tomography) imaging at 1 h and 24 h post-infusion (pi). Imaging results were subsequently validated by ex-vivo biodistribution.

Results Intravenous administration of $^{89}ZrNB(DFO)_2$ and $^{89}ZrG4(DFO)_3(Bdiol)_{110}$ resulted in their negligible brain accumulation regardless of BBB status and timing of OBBBO. Intra-arterial (IA) administration of $^{89}ZrNB(DFO)_2$ dramatically increased its brain uptake, which was further potentiated with prior OBBBO. Half of the initial brain uptake was retained after 24 h. In contrast, IA infusion of $^{89}ZrG4(DFO)_3(Bdiol)_{110}$ resulted in poor initial accumulation in the brain, with complete clearance within 1 h of administration. Ex-vivo biodistribution results reflected those on PET-CT.

Conclusions IA delivery of nanobodies might be an attractive therapeutic platform for CNS disorders where prolonged intracranial retention is necessary.

Keywords PET · Nanobody · Dendrimer · Intra-arterial · Zirconium · Brain

This article is part of the Topical Collection on Neurology

Wojciech G. Lesniak and Chengyan Chu contributed equally to this work.

Electronic supplementary material The online version of this article (https://doi.org/10.1007/s00259-019-04347-y) contains supplementary material, which is available to authorized users.

✉ Wojciech G. Lesniak
wlesnia1@jhmi.edu

✉ Miroslaw Janowski
mjanows1@jhmi.edu

[1] The Russell H. Morgan Department of Radiology and Radiological Science, Johns Hopkins University School of Medicine, Baltimore, MD, USA

[2] Institute for Cell Engineering, Johns Hopkins University School of Medicine, Baltimore, MD, USA

[3] Department of Biomolecular Medicine, Faculty of Medicine and Health Sciences, Ghent University, Ghent, Belgium

[4] Department of Radiology, Centre of Postgraduate Medical Education, Warsaw, Poland

Introduction

Neurological disorders and cerebral malignancies continue to be a significant burden to the society, in part due to the blood–brain barrier (BBB), which limits access for most drugs circulating in the blood, precluding them from reaching therapeutic concentrations in the central nervous system (CNS) [1]. Importantly, another relevant function of BBB is active efflux of molecules from the CNS [2]. Therefore, parenchymal accumulation of neurotherapeutic agents is contingent upon both penetration to the CNS and circumvention of clearance by the BBB. There are several methods to increase permeability and drug transport across the BBB; however, strategies to overcome drug clearance by BBB are less explored [3]. Low molecular weight and lipophilic molecules have been considered as most suitable for therapy of CNS disorders [4]; however, they have fallen short, necessitating alternative approaches.

Advances in biotechnology enable efficient and cost-effective design of macromolecules including antibodies, nanobodies, fusion proteins, and synthetic nanoparticles. Such scaffolds can be designed with high affinity and specificity for safe engagement of certain molecular targets [5]. These advances can also be applied to CNS therapeutics. We have recently shown that systemically infused anti-VEGF monoclonal antibody (bevacizumab) failed to accumulate in the brain, even upon osmotic blood–brain barrier opening (OBBBO) [6]. Transporter-based delivery of intravenously (IV)-administrated antibodies to the brain increased their uptake by an order of magnitude [7]. Intra-arterial (IA) delivery of bevacizumab, however, resulted in significant accumulation in the brain as measured by positron emission tomography (PET) (~10% of injected dose per cubic centimeter of tissue, %ID/cc), which was further increased by OBBBO to ~25 %ID/cc, several orders of magnitude higher than for systemic (IV) delivery [6]. Importantly, retention of bevacizumab in the brain after 24 h was high, which makes IA delivery of antibodies an attractive strategy, especially as the precision of endovascular infusions has been significantly improved by real-time guidance through magnetic resonance imaging (MRI) [8, 9]. We have recently applied this approach clinically in a patient with aggressive recurrent glioblastoma multiforme, and IA injection of bevacizumab, which resulted in a rapid therapeutic response [10].

While antibodies are quickly emerging as therapeutic agents, and demonstrated efficacy of their IA delivery to the CNS is an important step towards treatment of neurological disorders and CNS malignancies, they are plagued with several disadvantages including relatively complex production, high cost, and immunogenicity. Accordingly, there is growing interest in nanobodies as therapeutic agents and dendrimers as drug nanocarriers. Nanobodies are derived from naturally occurring heavy chain antibodies in camelids. They are one-tenth (~15 kDa) of the size of monoclonal antibodies. The small size of nanobodies has several advantages such as easy in-vitro production, lack of immune recognition, high affinity to molecular targets, and improved permeability across biological barriers [11, 12]. Furthermore, nanobody cDNAs are routinely produced, which opens opportunities for derivatization with fluorophores or anti-cancer therapeutics. Polyamidoamine (PAMAM) dendrimers are quickly emerging as a versatile nanoplatform for selective drug delivery due to their unique physicochemical properties, including small size, large number of reactive terminal groups that can be readily modified with different functionalities, bulky interior void volume, and biocompatibility [13, 14]. There have been reports of PAMAM dendrimers that cross the BBB upon IV administration, and their selective uptake by activated microglia in an experimental model of cerebral palsy [15, 16]. Another report involves accumulation of dendrimers within intracranial tumor-associated macrophages in a rodent model of gliosarcoma [17]. A generation-4 PAMAM dendrimer has a similar size to a nanobody and has the further advantage of capacity for conjugation with various functionalities, including ligands for molecular targets, imaging-radio-, chemo-, and immunotherapeutic agents [18]. Potential benefits of IA delivery of nanobodies and dendrimers over IV administration have not been assessed until now. Here, we measure the ability for nanobodies and generation-4 PAMAM hydroxy terminated dendrimers to penetrate and clear from the CNS using PET. In our study, neither nanobody nor dendrimer have specific targets in the brain, to provide basal kinetics for future studies with brain-targeted molecules and molecular targets in specific neurological diseases.

Materials

All chemicals were purchased from Sigma–Aldrich (Milwaukee, WI, USA) or Fisher Scientific (Tewksbury, MA, USA) unless otherwise specified. Ethylenediamine core amine-terminated generation-4 poly(amidoamine dendrimer) [G4(NH_2)$_{64}$] was acquired from Dendritech (Midland, MI, USA). $^{89}Zr(C_2O_4)_2$ ($t_{1/2}$ = 78.4 h) and 1-(4-isothiocyanatophenyl)-3-[6,17-dihydroxy-7,10,18,21-tetraoxo-27-(N-acetylhydroxylamino)-6,11,17,22-tetraazaheptaeicosine] thiourea (p-SCN-Bn-DFO, Cat. # B-705) were obtained from Washington University (St. Louis, MO, USA) and Macrocyclics (Plano, TX, USA),

respectively. All reagents and solvents were used as received without further purification.

Nanobody

Gelsolin nanobody 11 (NB11), cloned in the pHEN6c vector, was purified from WK6 cells as described previously [19]. Briefly, competent WK6 cells were transformed with the plasmid and grown at 37 °C in TB medium with 100 μg/ml ampicillin until the OD_{600} reached 0.60–0.80. Then temperature was set to 20 °C and nanobody expression was induced by the addition of 0.5 mM IPTG. After overnight induction, bacterial cultures were pelleted by centrifugation at 11,000×*g* for 20 min at 4 °C. Cells were resuspended in a small volume of phosphate-buffered saline (PBS), and 0.2 mg/ml lysozyme was added. Lysis proceeded during 30 min rotation at room temperature. This suspension was then sonicated (Vibracell, Sonics and Materials, Newtown, CT, USA) and centrifuged again (~29,000×*g*) for 30 min at 4 °C to obtain the bacterial protein lysate. The His_6-tagged nanobody was purified by Immobilized metal ion affinity chromatography (IMAC) on a Ni^{2+} column and eluted with 500 mM imidazole. Finally, nanobody 11 was purified to homogeneity by gel filtration chromatography on a Superdex 200 HR 10/30 column (GE Healthcare, Diegem, Belgium), equilibrated in 20 mM Tris.HCl pH 7.5, 150 mM NaCl, 1 mM DTT. *Composition of NB11:* Ala (11, 8.6%), Arg (9, 7.0%), Asn (4, 3.1%), Asp (9, 7.0%), Cys (2, 1.6%), Gln (9, 7.0%), Glu (3, 2.3%), Gly (14, 10.9%), His (1, 0.8%), Ile (2, 1.6%), Leu (7, 5.5%), Lys (4, 3.1%), Met (3, 2.3%), Phe (5, 3.9%), Pro (4, 3.1%), Ser (16, 12.5%), Thr (9, 7.0%), Trp (2, 1.6%), Tyr (5, 3.9%), Val (9, 7.0%). *Physicochemical properties:* total number of negatively charged residues (Asp + Glu) 12, total number of positively charged residues (Arg + Lys) 13, grand average of hydropathicity (GRAVY) 0.534, aliphatic index 56.41. Biological properties: the estimated half-life 30 h (mammalian reticulocytes, in vitro), > 20 h (yeast, in vivo), > 10 h (*Escherichia coli*, in vivo).

Synthesis of $NB(DFO)_2$

For conjugation of DFO with nanobody, storage buffer was replaced with saline using ultrafiltration with Millipore Amicon Ultra Centrifugal Filters 3000 Da molecular weight cut-off (MWCO, Millipore Sigma, cat #: UFC80030) and pH was adjusted to 9 with a small amount of 2 M Na_2CO_3 solution. Then five-fold molar equivalent of SCN-Bn-DFO dissolved in DMSO was added and conjugation was carried out for 30 min at 37 °C in a thermomixer at 550 r.p.m. Resulting NB-DFO conjugate was purified as described above, reconstituted in saline at 10 mg/ml and 0.1 ml aliquots were kept at −20 °C until further use.

Synthesis of $G4(DFO)_3(Bdiol)_{110}$ dendrimer

Preparation of $G4(DFO)_3(Bdiol)_{110}$ involved a one-pot, two-step synthesis as presented in Fig. 4. $G4(NH_2)_{64}$ dendrimer (0.030 g, 2.11×10^{-6} mol) was dissolved in 3 ml deionized water resulting in pH = 9.2 and 5 mol equivalent of SCN-Bn-DFO (0.008 g, 1.05×10^{-5} mol) reconstituted in 0.2 ml of DMSO was added. The reaction proceeded for 30 min at 37 °C in a thermomixer at 550 r.p.m., and a small amount of reaction mixture was subjected to MALDI-TOF mass spectrometry to confirm conjugation of DFO with dendrimer. Next, 0.2 ml (2.99×10^{-3} mol) of glycidol was added and reaction was carried for additional overnight to cap remaining primary amines with butane-1,2-diol (Bdiol). Resulting $G4(DFO)_3(Bdiol)_{110}$ dendrimer was purified using deionized water and ultrafiltration with Millipore Amicon Ultra Centrifugal Filters 10,000 Da MWCO, lyophilized, yielding 0.035 g of the conjugate, which was stored at −20 °C until further use.

Matrix-assisted laser desorption ionization-time-of-flight (MALDI-TOF)

To determine average number of DFO molecules conjugated with nanobody and dendrimer and assess its capping efficiency with butane-1,2-dio, MALDI-TOF spectra were recorded on a Voyager DE-STR spectrophotometer, using 2,5-dihydroxybenzoic acid (DHB) as a matrix, which was dissolved in 50% MeOH and 0.1% TFA aqueous solution at concentration of 20 mg/ml. NB and $NB(DFO)_2$ samples were desalted using Zeba™ spin columns 7 K MWCO (cat. # 89882, Thermo Fisher Scientific). Samples of $G4(NH_2)_{64}$, $G4(NH_2)_{61}(DFO)_3$, and $G4(DFO)_3(Bdiol)_{110}$ dendrimers were prepared in deionized water. 10 μl of samples were mixed with 10 μl of matrix, and 1 μl of resulting mixture was placed on the target plate (in triplicate) and evaporated. Number of shots and laser power was adjusted according to spectrum quality.

Dynamic light scattering and zeta potential analysis

Dynamic light scattering and zeta potential analyses were performed using a Malvern Zetasizer Nano ZEN3600. $G4(DFO)_3(Bdiol)_{110}$ dendrimer was prepared at a concentration of 4 mg/ml in PBS (c = 0.1 M, pH 7.4). DLS measurements were performed at a 90° scattering angle at 25 °C. Zeta potential analysis was carried out using the same solution.

Radiolabeling of $NB(DFO)_2$ and $G4(DFO)_3(Bdiol)_{110}$

Radiolabeling of $NB(DFO)_2$ and $G4(DFO)_3(Bdiol)_{110}$ with ^{89}Zr was performed using reported procedure [20]. $^{89}ZrNB(DFO)_2$ was fabricated with ~99% radiochemical

purity and 129.5 ± 10 MBq/mg specific activity. ^{89}ZrG4(DFO)$_3$(Bdiol)$_{110}$ was prepared with ~99% radiochemical purity and 120 ± 8 MBq/mg specific activity. For further studies, ^{89}ZrNB(DFO)$_2$ and ^{89}ZrG4(DFO)$_3$(Bdiol)$_{110}$ were diluted with sterile saline.

Partition coefficient of ^{89}ZrNB(DFO)$_2$ and ^{89}ZrG4(DFO)$_3$(Bdiol)$_{110}$

To vials containing 0.5 ml PBS (pH 7.4), 0.5 ml of octanol, 0.74 MBq of ^{89}ZrNB(DFO)$_2$ or ^{89}ZrG4(DFO)$_3$(Bdiol)$_{110}$ was added (n = 3). Resulting solutions were vortexed vigorously for 3 min. Then to achieve efficient phase separation, vials were centrifuged for 5 min at 4000×g. Aliquots (100 μl) of the aqueous and the octanol phase were collected and the radioactivity in the respective samples were measured using a PerkinElmer - 2480 Automatic Gamma Counter (Waltham, MA). The LogP values were calculated from the means of n = 3 separate measurements.

PET-CT imaging of IA and IV delivery of ^{89}ZrNB(DFO)$_2$ and ^{89}ZrG4(DFO)$_3$(Bdiol)$_{110}$ with or without OBBBO

PET-CT studies were performed as we have recently described [6] using 6–8-week-old male C3HeB/FeJ mice (stock number 000658; Jackson, n = 4 per group, total n = 28). Under general anesthesia, a catheter was placed in the internal carotid artery (ICA), as we have reported previously [21] and mice were transferred to the PET-CT scanner. BBB opening was performed with 25% mannitol infused for 1 min at a speed of 0.15 ml/min. Speed of mannitol infusion to achieve reproducible BBB opening in mice was optimized in our previous study [21]; ~8.5 MBq (~230 μCi) of ^{89}ZrNB(DFO)$_2$ or ^{89}ZrG4(DFO)$_3$(Bdiol)$_{110}$ reconstituted in 1 ml of saline was infused IA or IV over 5 min at 0.15 ml/min flow rate. There were four experimental groups: 1) IA infusion with BBB intact (IA/BBBI), 2) OBBBO followed by IA infusion (OBBBO/IA), 3) OBBBO followed by intravenous infusion (OBBBO/IV) and 4) intravenous infusion followed by OBBBO (IV/OBBBO) for ^{89}ZrNB(DFO)$_2$. Three groups — 1) IA infusion with BBB intact (IA/BBBI), 2) OBBBO followed by IA infusion (OBBBO/IA), and 3) intravenous infusion followed by OBBBO (IV/OBBBO) — were evaluated for ^{89}ZrG4(DFO)$_3$(Bdiol)$_{110}$. Accumulation of ^{89}ZrNB(DFO)$_2$ or ^{89}ZrG4(DFO)$_3$(Bdiol)$_{110}$ in the brain was initially evaluated with dynamic 30-min-long PET scans divided into 30 s frames, followed by whole body PET/CT imaging acquired around 1 h and 24 h post-infusion (pi), in two bed positions and 7 min per bed on an ARGUS small-animal PET/CT scanner (Sedecal, Madrid, Spain). A CT scan (512 projections) was performed before whole-body PET imaging at 1 h (mice remained in the scanner after dynamic scan was completed) and 24 h pi, to enable co-registration. PET data were reconstructed using the two-dimensional ordered subsets-expectation maximization algorithm (2D-OSEM), and corrected for dead time and radioactive decay. Presented whole-body images were generated using Amira® (FEI, Hillsboro, OR, USA) and dynamic scans (brain and heart radioactivity accumulation) and radioactivity distribution in different brain regions were analyzed with PMOD 4.3 (PMOD Technologies LLC, Zürich, Switzerland). The peak concentration of radioactivity over 5 min around the end of IA infusion of ^{89}ZrNB(DFO)$_2$ and ^{89}ZrG4(DFO)$_3$(Bdiol)$_{110}$ was extracted, and compared with the last 5 min of the dynamic scans to calculate the rate of early clearance of administrated radiotracers from the brain. Then the radioactivity detected in the CNS at 1 h and 24 h after infusion was used to assess their later brain clearance. The effect of OBBBO on nanobody or dendrimer brain accumulation following their IV infusion was evaluated by comparing level of radioactivity 5 min before and 5 min after mannitol administration.

Ex-vivo biodistribution of ^{89}ZrNB(DFO)$_2$ and ^{89}ZrG4(DFO)$_3$(Bdiol)$_{110}$

Upon completion of PET-CT at 24 h pi of ^{89}ZrNB(DFO)$_2$ or ^{89}ZrG4(DFO)$_3$(Bdiol)$_{110}$, mice were sacrificed; blood, brain (divided into right and left hemispheres), and selected organs were harvested and weighed. The radioactivity in collected samples was measured on a PerkinElmer 2480 Automatic Gamma Counter (Waltham, MA, USA) 4 days after sample collection to avoid detector saturation due to high radioactivity accumulation in brain and kidneys. To calculate the percent of injected dose per gram of tissue (%ID/g), triplicate radioactive standards (0.01% of the injected dose) were counted along with tissue samples. Biodistribution data shown is mean ± the standard deviation (SD).

Statistical analysis

PROC MIXED (SAS 9.4) was used for statistical analysis, with the lowest means square (LMS) test for comparison between groups [22]. The statements “repeated” and “random” were used for repeated measures and to express random effects, respectively.

Results

Synthesis of ^{89}ZrNB(DFO)$_2$

Preparation of ^{89}ZrNB(DFO)$_2$ involved conjugation of on average two DFO molecules as measured by MALDI-TOF spectrometry (Fig. S1) and subsequent radiolabeling with Zirconium-89 (Fig. 1). Partition coefficient analysis provided a LogP value of −2.35 for ^{89}ZrNB(DFO)$_2$, indicating that the

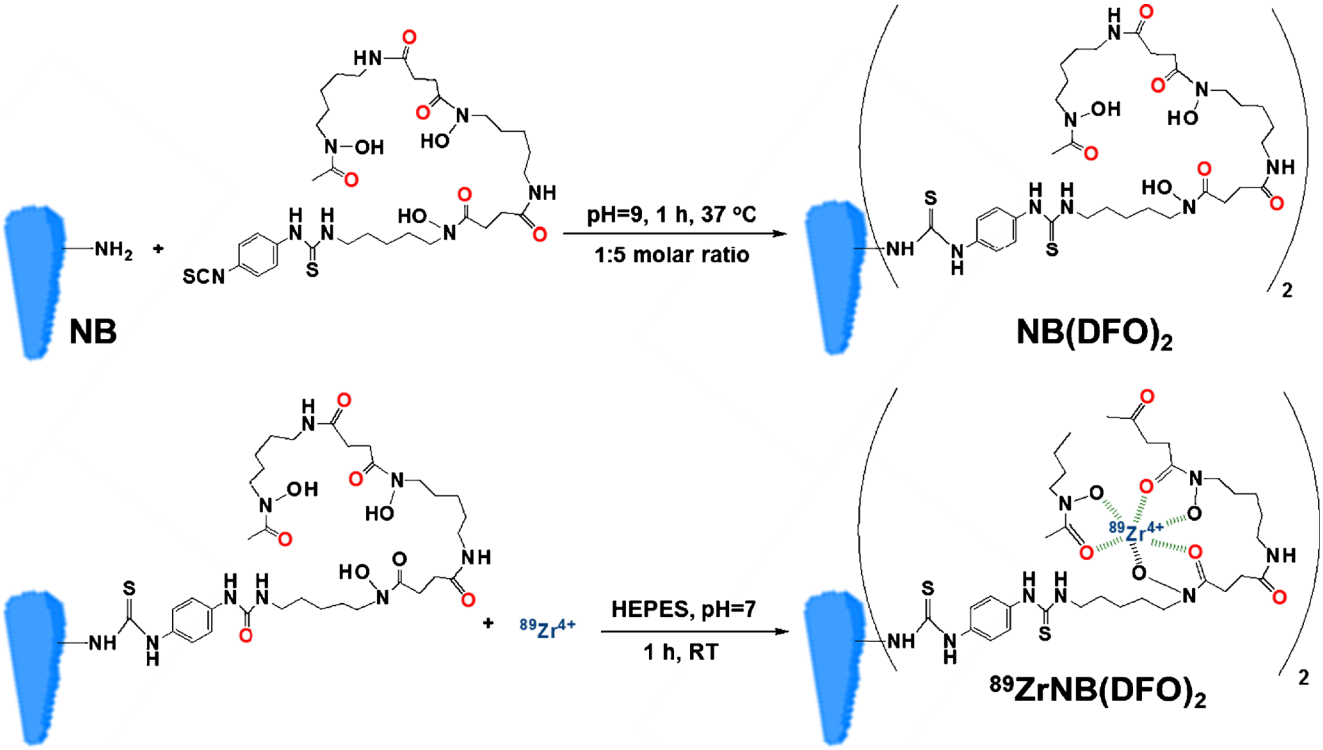

Fig. 1 Conjugation of nanobody with DFO and radiolabeling with ^{89}Zr

nanobody is hydrophilic, in agreement with the theoretically estimated GRAVY of −0.534 and graph of theoretical hydrophilicity, showing that most of the NB11 molecule is hydrophilic (Fig. S2).

CNS uptake of ^{89}ZrNB(DFO)$_2$ and its biodistribution

Nearly linear uptake of radioactivity in the ipsilateral hemisphere was observed during IA infusions of ^{89}ZrNB(DFO)$_2$ regardless of the BBB status, with no accumulation in the contralateral hemisphere (Fig. 2). The IA/BBBI infusion resulted in ^{89}ZrNB(DFO)$_2$ accumulation in the ipsilateral hemisphere with a peak concentration of 25.79 ± 15.79 %ID/cc, and OBBBO further enhanced its uptake to 60.66 ± 35.41 %ID/cc ($P < 0.05$). Radioactivity in the CNS after IV infusion of ^{89}ZrNB(DFO)$_2$ was at background level regardless of the timing of OBBBO. The background radioactivity after OBBBO/IV and IV/OBBBO remained at a similar level during dynamic scans and in subsequent whole-body PET-CT imaging. For clarity we are not presenting those separately. There was very slow early clearance of radioactivity from the ipsilateral hemisphere over a period of 30 min, which was not significant for IA/BBBI (22.46 ± 15.05, P = NS), but it was statistically different for OBBBO/IA infusion (53.66 ± 30.73, $P < 0.05$). The whole-body PET-CT imaging performed 1 h after infusion revealed a similar pattern of radioactivity uptake in the brain as at the end of the dynamic PET scan, which then decreased nearly by 50%, 24 h after infusion ($P < 0.05$, Fig. 3, Table 1). In all evaluated cohorts, high uptake of radioactivity was also observed in kidneys, indicating renal clearance (Fig. 3 and Table 1). High accumulation of ^{89}ZrNB(DFO)$_2$ in the ipsilateral hemisphere upon OBBBO/IA infusion resulted in its statistically relevant lower concentration in kidneys at 1 h after infusion (26.72 ± 4.19) in comparison to IA/BBBI (43.36 ± 3.83) and IV/OBBBO (39.61 ± 7.51 %ID/cc). The clearance of ^{89}ZrNB(DFO)$_2$ from brain over 24 h resulted in increase of radioactivity in kidneys to 35.38 ± 5.11 %ID/cc in OBBBO/IA group ($P < 0.05$), while no difference was observed for the remaining experimental groups (41.84 ± 5.47 and 40.34% ± 7.91 %ID/cc for IA/BBBI and IV/OBBBO respectively). For IV/OBBBO, 12.48 ± 2.32 %ID/cc of ^{89}ZrNB(DFO)$_2$ could also be detected in the lungs 1 h after infusion. In agreement with PET-CT imaging, post-mortem biodistribution analysis (Fig. 3) revealed significantly higher accumulation of ^{89}ZrNB(DFO)$_2$ in the ipsilateral hemisphere in OBBBO/IA (17.8 ± 5.99 %ID/g) compared to IA/BBBI (6.15 ± 3.53 %ID/g), and IV/OBBBO (0.09 ± 0.03 %ID/g) infusions with negligible radioactivity uptake in the contralateral hemispheres in all mice 24 h after infusion. Among peripheral organs, the highest accumulation of ^{89}ZrNB(DFO)$_2$ was detected in kidneys followed by the spleen, liver, and lungs in all evaluated groups.

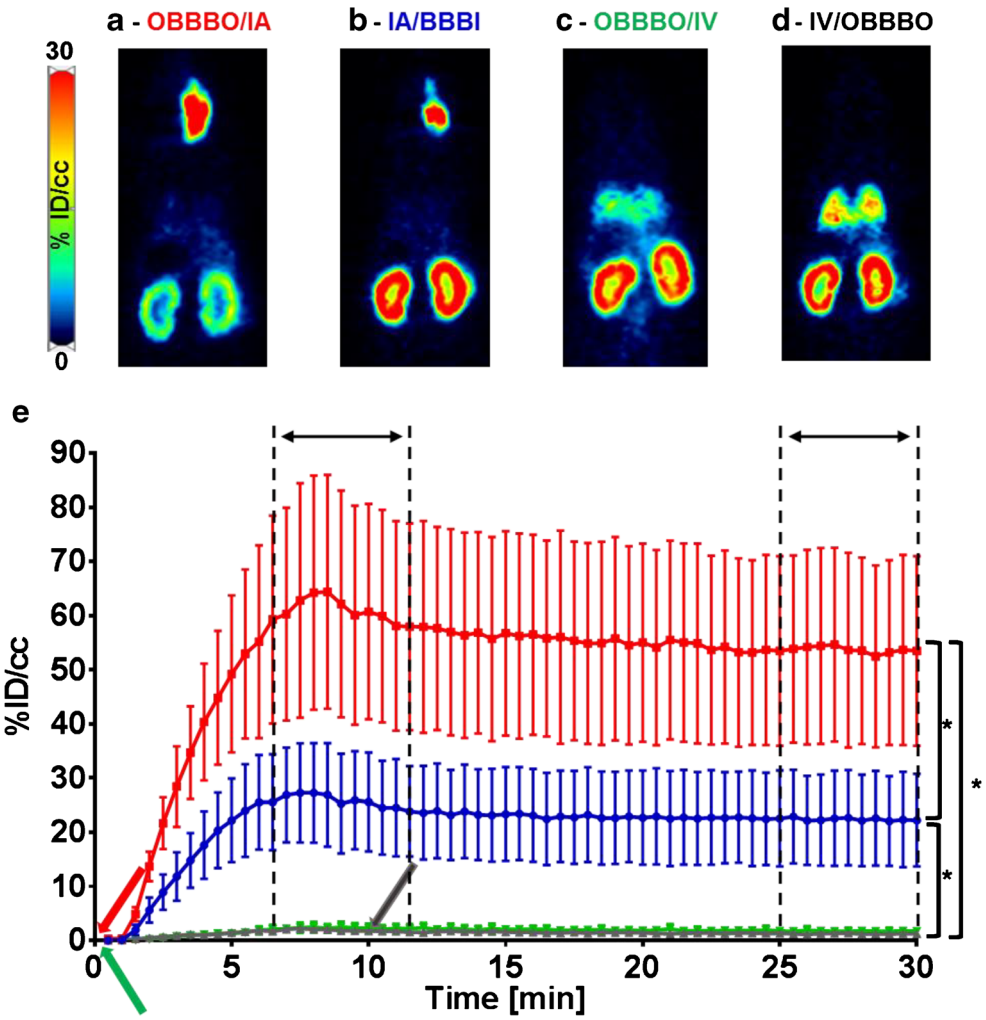

Fig. 2 PET imaging and dynamics of [^{89}Zr]NB(DFO)$_2$ uptake in ipsilateral hemisphere. Representative coronal PET images recorded 1 h after infusion, illustrating brain uptake of ^{89}ZrNB(DFO)$_2$ upon: **a** OBBBO followed by immediate IA infusion of 8.5 MBq of ^{89}ZrNB(DFO)$_2$ reconstituted in 1 ml of saline at 0.15 ml/min; **b** IA infusion with BBBI; **c** OBBBO followed by immediate IV infusion; and **d** IV infusion followed by OBBBO at 5 min after radiotracer administration was completed, showing the highest accumulation of radioactivity in ipsilateral hemisphere upon OBBBO/IA; **e** curves demonstrating dynamics of ^{89}ZrNB(DFO)$_2$ uptake in the ipsilateral hemisphere upon OBBBO/IA (*red line*), IA/BBBI (*blue line*), OBBBO/IV (*green line*) and IV/OBBBO (*gray line*; *arrows* show time of OBBBO) indicating highest brain uptake of ^{89}ZrNB(DFO)$_2$ in animals treated with OBBBO and IA infusion and lack of its brain accumulation upon IV administration regardless timing of OBBBO. Each time point is presented as mean and SEM, $n = 4$

Synthesis of ^{89}ZrG4(DFO)$_3$(Bdiol)$_{110}$

G4(NH$_2$)$_{64}$ was conjugated with a average of three molecules of DFO (Fig. 4), and remaining primary amines were substituted with 110 butane-1,2-diol moieties, as assessed by increase of the molecular weight observed in MALDI-TOF spectrometry (Fig. S3A). A one-pot synthesis yielded nanoparticles with narrow size distribution around 5 nm (Fig. S3B) and neutral net-surface charge, indicated by zeta potential of −1.8 mV. Resulting G4(DFO)$_3$(Bdiol)$_{110}$ dendrimer was subsequently radiolabeled with ^{89}Zr, and the LogP of −2.84 was measured for resulting ^{89}ZrG4(DFO)$_3$(Bdiol)$_{110}$, confirming it is hydrophilic.

CNS uptake of ^{89}ZrG4(DFO)$_3$(Bdiol)$_{110}$ and its biodistribution

There was no difference in the peak concentration of ^{89}ZrG4(DFO)$_3$(Bdiol)$_{110}$ in the ipsilateral hemisphere for IA/BBBI (3.29 ± 1.31%ID/cc) and OBBBO/IA (3.20 ± 1.47 %ID/cc) infusions (P = NS) as indicated by the time–activity curves and PET images obtained by summing frames collected between 5 and 10 min of dynamic scans (Fig. 5). This low accumulation of dendrimer in the brain was despite BBB opening at the time of maximum ^{89}ZrG4(DFO)$_3$(Bdiol)$_{110}$ concentration in the blood pool (Fig. 5a). We did not evaluate the effect of OBBBO prior to IV infusion of dendrimers as for nanobodies. IV/OBBBO infusion resulted in a background radioactivity uptake of 1.22 ± 0.29 %ID/cc in the CNS, with decrease of radioactivity after OBBBO to 1.1 ± 0.25 ($P < 0.05$). The fast and statistically significant clearance of ^{89}ZrG4(DFO)$_3$(Bdiol)$_{110}$ from the brain was observed regardless of BBB status, reaching 1.68 ± 0.8, 1.05 ± 0.22, 0.and 83 ± .018 %ID/cc for OBBBO/IA, IA/BBBI, and BBBO/IV respectively, at the end of the dynamic PET scan. However, the clearance after OBBBO/IA was somewhat slower compared to IA/BBBI ($P < 0.05$). IA/BBBI actually dropped to the same low level as IV/OBBBO (P = NS) at the end of the dynamic scans. However, whole-body PET-CT imaging performed 1 h after infusion showed only background radioactivity in the brain

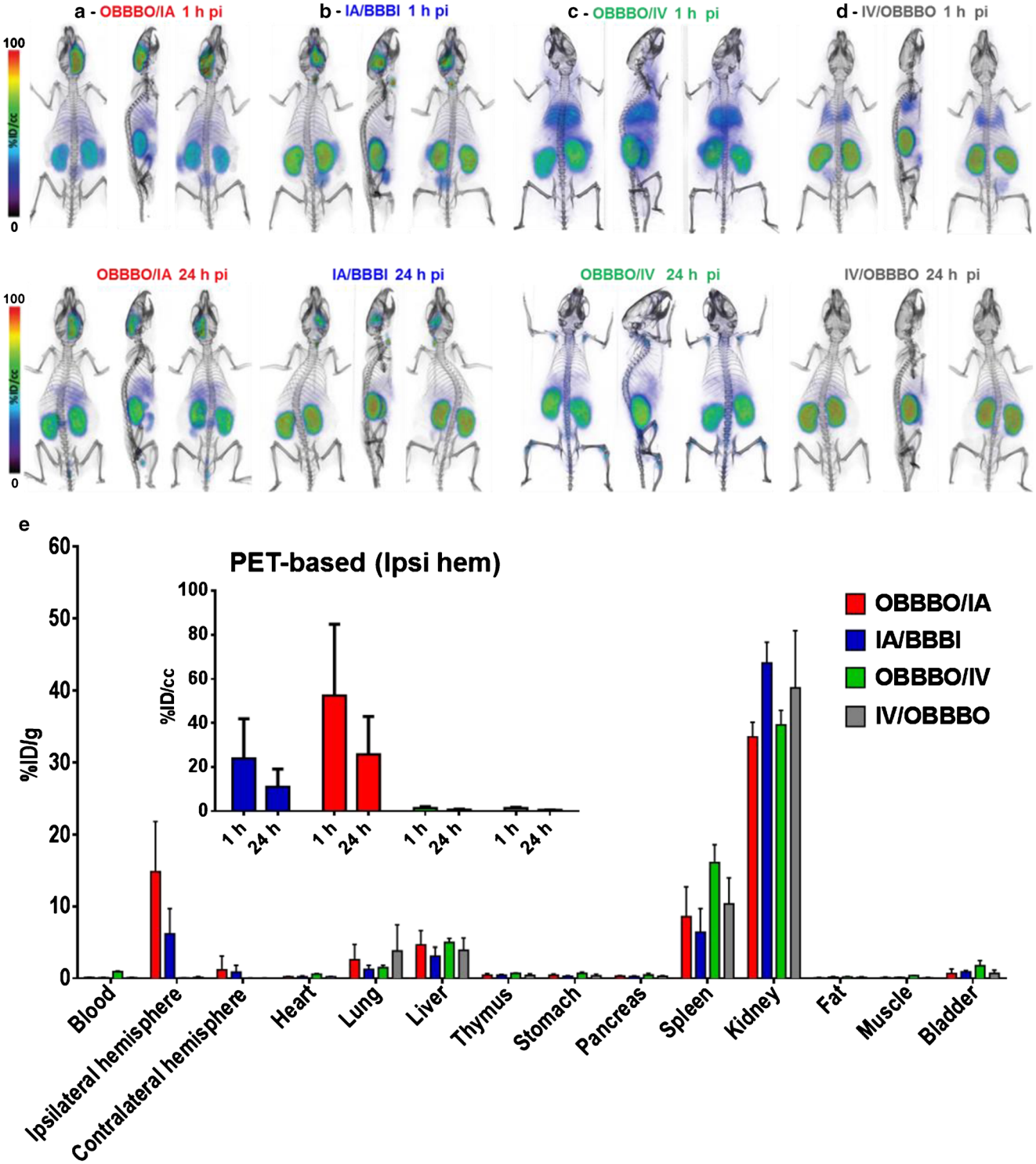

Fig. 3 PET-CT imaging and ex-vivo biodistribution of ^{89}ZrNB(DFO)$_2$ at 24 h after infusion. Whole body volume rendered PET-CT images recorded 1 h and 24 h post infusion of ~8.5 MBq (~230 μCi) of ^{89}ZrNB(DFO)$_2$, demonstrating its biodistribution upon: **a** OBBBO followed by immediate IA infusion; **b** IA infusion with BBBI; **c** OBBBO followed by immediate IV infusion; and **d** IV infusion followed by OBBBO 5 min after infusion was completed. **e** Ex-vivo biodistribution of ^{89}ZrNB(DFO)$_2$ at 24 h after infusion in the same groups (*insert* - PET-based quantification of ^{89}ZrNB(DFO)$_2$ uptake in ipsilateral hemisphere), showing in agreement with PET imaging higher uptake of ^{89}ZrNB(DFO)$_2$ in ipsilateral hemisphere compared to contralateral hemisphere in OBBBO/IA group and its higher brain accumulation in comparison with IA/BBBI, OBBBO/IV, and IV/OBBBO cohorts

regardless of the route of ^{89}ZrG4(DFO)$_3$(Bdiol)$_{110}$ delivery, with no statistically significant differences among groups (Fig. 5c and 6). Significant amounts of radioactivity could be detected in kidneys and bladder, followed by

Table 1 PET-based assessment of ^{89}ZrG4(DFO)$_3$(Bdiol)$_{110}$ biodistribution

	AI/OBBBO (%ID/cc)	IA/BBBI (%ID/cc)	IV/BBBO (%ID/cc)
1 h after infusion			
Ipsilateral hemisphere	1.9 ± 0.74	1.23 ± 0.33	1.31 ± 0.21
Kidneys	31.09 ± 1.33	66.48 ± 3.51	47.74 ± 2.62
Bladder	35.24 ± 1.85	26.46 ± 15.09	39.38 ± 5.95
Liver	15.82 ± 1.22	26.47 ± 7.48	15.33 ± 0.87
24 h after infusion			
Kidneys	18.61 ± 1.22	21.67 ± 1.59	19.68 ± 1.57
Liver	13.01 ± 2.01	13.91 ± 1.69	12.35 ± 1.56

liver at 1 h after infusion, indicating renal clearance with hepatic involvement. At 24 h after infusion, no radioactivity in the brain of evaluated mice was observed. In agreement with PET-CT imaging, post-mortem biodistribution demonstrated negligible accumulation of ^{89}ZrG4(DFO)$_3$(Bdiol)$_{110}$ in both hemispheres (P = NS) and presence of radioactivity in kidneys and liver for all assessed delivery routes (Fig. 6). Twenty-four hours after infusion, tracer retention in the ipsilateral hemisphere and bladder was below PET quantification limit.

Discussion

We have shown that the IA route was more effective in delivering nanobodies to the brain than systemic administration, regardless of the BBB status. Preceding OBBBO potentiated brain accumulation of the nanobodies by ~2.5-fold. Brain uptake of ^{89}ZrNB(DFO)$_2$ reached 60.66 ± 35.41 %ID/cc, which is higher compared to brain accumulation of 23.58 ± 4.58 %ID/cc for ^{89}Zr radiolabeled-bevacizumab (^{89}ZrBVDFO) observed in our previous study [6]. While half of the ^{89}ZrNB(DFO)$_2$ was cleared from the brain over 24 h, clearance of ^{89}ZrBVDFO was slower. In both studies, bevacizumab and the nanobody did not have specific targets in mouse brains. Brain retention of generation-4 hydroxy terminated PAMAM dendrimer was marginal. The peak concentration of ^{89}ZrG4(DFO)$_3$(Bdiol)$_{110}$ in the brain was only 3 %ID/cc after IA delivery regardless of BBB status, decreasing to background levels within 1 h. Intravenous infusion of ^{89}ZrNB(DFO)$_2$ and ^{89}ZrG4(DFO)$_3$(Bdiol)$_{110}$ resulted in only background tracer retention regardless of BBB status. Our results are in agreement with previous reports showing negligible penetration of PAMAM dendrimers through intact BBB upon IV administration, regardless of their size and terminal functionalities, including hydroxy, carboxyl, and polyethylene glycol groups [23–25]. Kannan et al. demonstrated uniform accumulation of Cy5 fluorescently labeled generation-4 hydroxy terminated PAMAM dendrimer in a rodent model of gliosarcoma, as well as its specific uptake by tumor-associated macrophages after systemic delivery [17]. Although microscopic imaging was convincing, the peak concentration of dendrimer in tumor reached only ~0.023 %ID/g at 8 h after injection and decreased to ~0.0067 %ID/g 40 h later, as measured by fluorescence spectroscopy of extracted tissue [17]. Similarly, very low brain uptake of ~0.07 %ID/g in neonatal rabbits with cerebral palsy and 0.003 %ID/g healthy control pups for the same dendrimer at 24 h after injection was also reported [26]. Both studies, in agreement with our results, demonstrated marginal BBB permeability and brain retention of generation-4 hydroxy terminated PAMAM dendrimers even with a compromised BBB, brain tumor, or activated

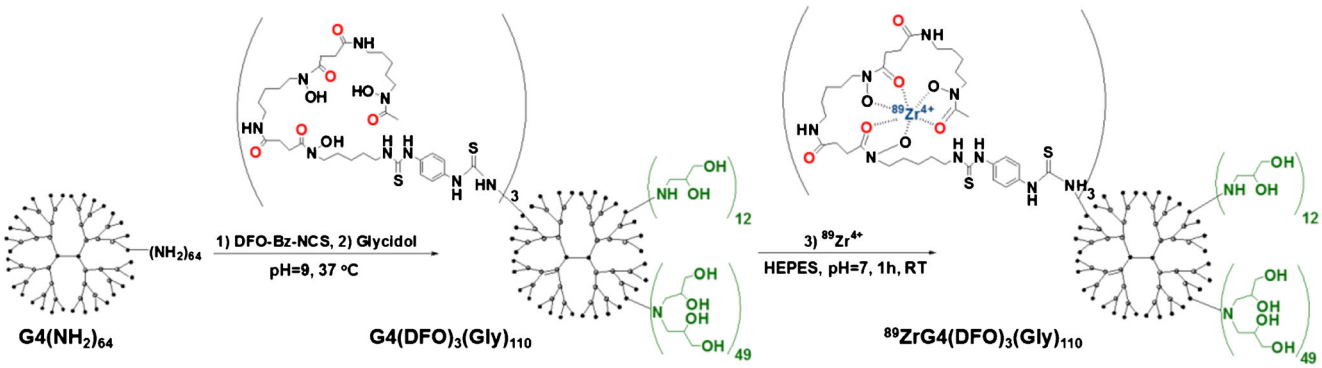

Fig. 4 Conjugation of G4(NH$_2$)$_{64}$ dendrimer with DFO, followed by capping of primary amines with butane-1,2-diol moieties and radiolabeling with ^{89}Zr

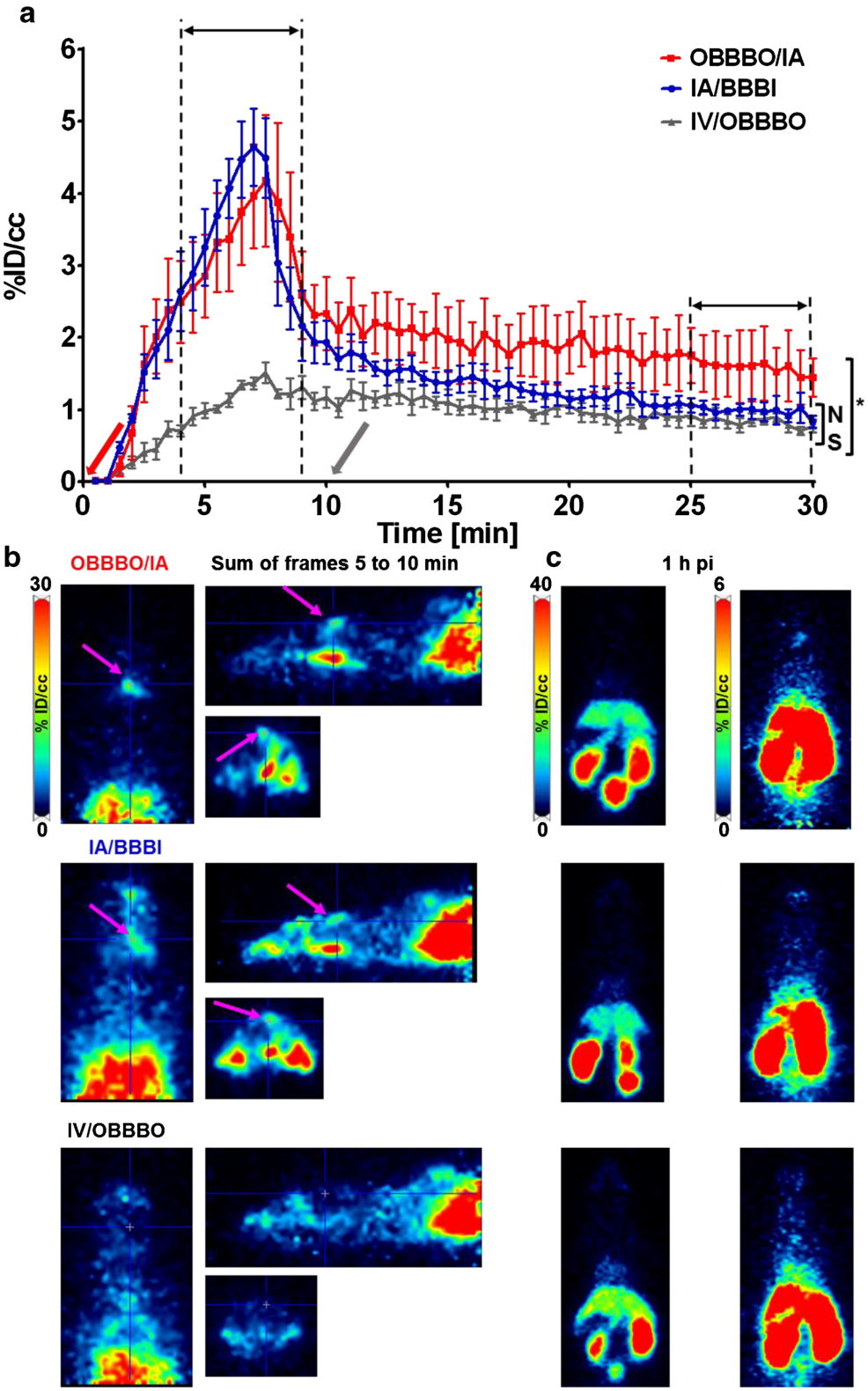

Fig. 5 Time–activity curves of ^{89}ZrG4(DFO)$_3$(Bdiol)$_{110}$ uptake in ipsilateral hemisphere and corresponding PET imaging. **a** Curves demonstrating dynamics of ^{89}ZrG4(DFO)$_3$(Bdiol)$_{110}$ accumulation in the ipsilateral hemisphere upon OBBBO/IA (*red line*), IA/BBBI (*blue line*), and IV/OBBBO (*gray line*; *arrows* show when BBB was opened) indicating significantly lower uptake compared to ^{89}ZrNB(DFO)$_2$ and no benefits of OBBBO application. Each time point is presented as mean and SEM, $n = 4$. **b** Representative orthogonal PET images obtained by summing frames between 5 and 10 min acquired during 30 min long dynamic scans. **c** Representative axial PET images with scales adjusted to demonstrate whole body distribution of radioactivity (*left panel*) and absence of ^{89}ZrG4(DFO)$_3$(Bdiol)$_{110}$ in the brain (*right panel*) 1 h after infusion. Results demonstrate negligible retention of ^{89}ZrG4(DFO)$_3$(Bdiol)$_{110}$ in the brain regardless of BBB status and route of administration

microglia present in cerebral palsy model. Interestingly, PET imaging of generation-4 hydroxy terminated dendrimer-radiolabeled with copper-64 in newborn rabbits with cerebral palsy indicated brain accumulation of radioactivity around 2.5 %ID/cc 24 h after injection [15]. However, copper-64 undergoes trans-chelation in vivo, in particular in the absence of a strong Cu(II) chelator forming thermodynamically stable complexes [27].

Our ^{89}ZrNB(DFO)$_2$ and ^{89}ZrG4(DFO)$_3$(Bdiol)$_{110}$ were not targeted to specific molecular species within the BBB or the brain. Also, no disease model was induced, enabling testing as a baseline therapeutic delivery platform for CNS drug delivery. In this context, the nanobodies seem attractive for IA infusion, while a lot of caution should be taken regarding utility of PAMAM dendrimers as drug delivery vehicles for brain diseases, especially when they are administered systemically. Therefore, in the case of PAMAM dendrimers the challenge for appropriate surface modification to achieve appreciate brain uptake and retention remains open. While here we tested generation-4 hydroxy terminated PAMAM dendrimers constructed by capping the primary amines with butane-1,2-diol, the same dendrimers with different surface modifications can potentially exhibit higher brain retention, and our study may serve as a benchmark for quantitative performance of dendrimer-based diagnostics and therapeutics in the CNS diseases. In contrast, the IA route is very effective in delivery of nanobodies, and their relatively fast clearance comparing to antibody could potentially be mitigated by applying nanobodies aimed for a specific brain target. While IV administration is highly ineffective for delivery of nanobodies to the brain, it was recently reported that the intranasal route might be an alternative [28]. However, no quantitative assessment of intranasal brain delivery of nanobodies has been reported yet. There is progress in design of nanobodies against brain disorders [29], and our IA infusion might be a right approach to use them effectively in the clinic. Especially after the anti-tumoral

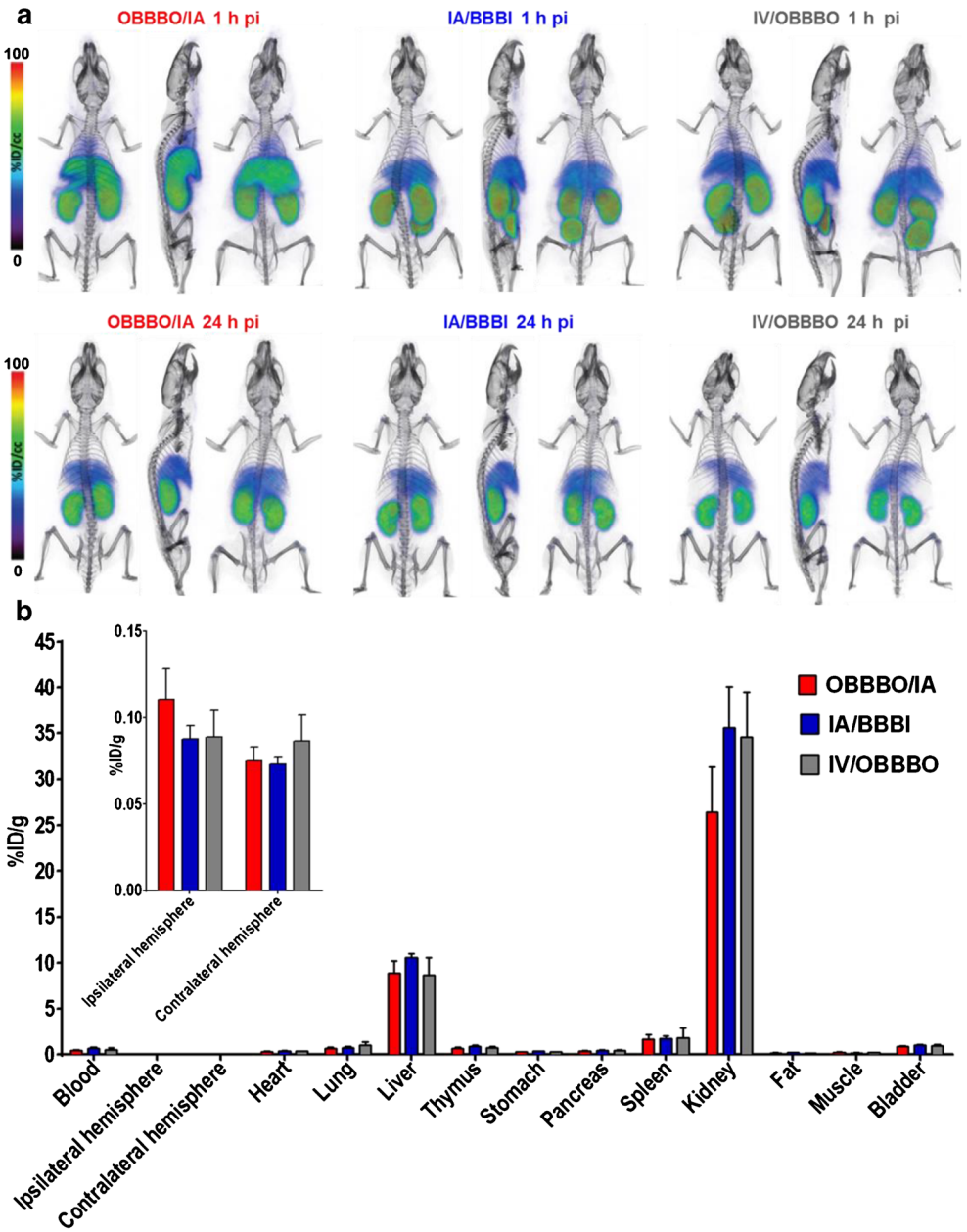

Fig. 6 PET-CT imaging and ex-vivo biodistribution of ^{89}ZrG4(DFO)$_3$(Bdiol)$_{110}$. **a** Representative whole body volume rendered PET-CT images recorded 1 h and 24 h post infusion of ^{89}ZrG4(DFO)$_3$(Bdiol)$_{110}$ for OBBBO/AI, AI/BBBI. and IV/OBBBO infusions. **b** Ex-vivo biodistribution of ^{89}ZrG4(DFO)$_3$(Bdiol)$_{110}$ at 24 h after infusion in the same mice (*insert* - scale was adjusted to show brain accumulation of ^{89}ZrG4(DFO)$_3$(Bdiol)$_{110}$, indication lack of ^{89}ZrG4(DFO)$_3$(Bdiol)$_{110}$ retention on the brain regardless of method of administration and its renal clearance with minor hepatic uptake

activity of neutralizing antibodies was shown in a mouse model of melanoma, the potentially neutralizing nanobodies could also be created against brain targets [30].

Limitations We have observed relatively high variability in brain uptake of nanobodies after IA delivery. We performed four rounds of experiments, in four groups of animals (IA/BBBI, OBBBO/IA, IV/OBBBO, and OBBBO/IV); and while we observed high reproducibility within rounds with relatively constant ratio of brain uptake OBBBO/IA versus IA/BBBI (ca. 2.5 x), relatively high variability between rounds was observed. No brain uptake and no variability was observed after IV delivery regardless of the timing of BBB opening. Interestingly, in one animal we observed the brain uptake at nearly 100 %ID/cc, which actually shows a high promise for the IA route and the possibility for further improvement of nanobody delivery to the brain. There might be various sources of variability including kinetics of cerebral blood flow or volume of the brain perfused from the IA catheter. It has been recently shown that real-time MRI can increase reproducibility of OBBBO [21]; thus, studies like ours would benefit from PET/MR systems, in which infusion parameters could be adjusted based on feedback from real-time MRI and quantitative assessment of brain uptake of infused molecules based on PET imaging. In a clinical setting, the real-time monitoring of IA delivery of nanobodies to the brain using PET, until the required quantity is achieved, might be an ultimate solution for precise dosing. In our study, we have not measured the affinity of radiolabeled nanobody, as we have not used it to bind a specific target, but it has previously been shown that nanobodies can be radiolabeled without losing their efficacy, providing a proof-of-concept for the viability of our approach [31, 32]. Also, we have not studied mechanisms behind such different penetration of BBB and brain retention of nanobodies vs dendrimers, which have similar basic physicochemical properties such as size, average charge, and hydrophilicity (Table S1). The drastically different in-vivo behavior of NB11 and $G4(DFO)_3(Bdiol)_{110}$ is most likely buried in their different structural composition. The studied nanobody was composed of a large number of amino acids with different side chains enforcing its folding and rigid 3D structure, forming fragments capable of, for example, electrostatic or hydrophobic interactions with biological species, as presented in Fig. S2, showing variable hydrophobicity along sequence of NB11. This may also be the case for antibodies that similarly to nanobodies result in high brain uptake after IA injection. On the contrary, polymeric $G4(DFO)_3(Bdiol)_{110}$ dendrimers, composed of ethane-1,2-diamine, butyraldehyde, and butane-1,2-diol are flexible and only have hydrophilic hydroxy groups in their surface, yielding molecules of highly uniform hydrophilicity. We also did not study compartmentalization or aggregation of nanobodies in the blood following IA administration, which could explain improved accumulation after IA delivery. Since the IV and IA infusion processes are identical in terms of the infusion speed and duration or catheter size, we did not expect aggregation before or after IA delivery, which could increase the retention in the brain at a cost of reducing biological activity. However, should aggregation have occurred, we would have observed substantial accumulation of the nanobody in the lungs after IV injection. We observed quite the opposite, as a large proportion of the nanobody was routed for renal clearance, as expected for monodispersed nanobodies. Nevertheless, follow-up experiments are warranted, and should be performed in the future to better understand the rules governing the advantages of IA delivery of macromolecules.

Conclusions

We have shown that brain delivery of nanobodies and generation-4 hydroxy terminated PAMAM dendrimers upon IV administration is negligible, regardless of BBB status. The IA route substantially increases brain uptake of nanobodies, which is further potentiated by OBBBO. However, half of the nanobodies are cleared from the brain within 24 h. Designing nanobodies against specific brain targets could ameliorate this deficiency. In contrast, the IA route marginally improved brain delivery of dendrimers, which quickly cleared from CNS. Appropriate surface modification of PAMAM dendrimers may improve their brain uptake and retention.

Funding This work was funded by National Institutes of Health (NIH) R01NS091110, R21NS106436, P41 EB024495.

Compliance with ethical standards

Disclosure of potential conflict of interest JAG has a financial and/or business interests in Gulliver Biomed BVBA, a company that licensed the tested nanobody; however, since the nanobody does not have a brain target there are no direct benefits to Gulliver Biomed. The remaining authors declared no conflict of interest related to the current work.

Ethical approval All animal procedures were carried out under protocols approved by the Johns Hopkins Animal Care and Use Committee. All applicable international, national, and/or institutional guidelines for the care and use of animals were followed. This article does not contain any studies with human participants performed by any of the authors.

References

1. Woodworth GF, Dunn GP, Nance EA, Hanes J, Brem H. Emerging insights into barriers to effective brain tumor therapeutics. Front Oncol. 2014;4:126. https://doi.org/10.3389/fonc.2014.00126.
2. Mayhan WG, Heistad DD. Permeability of blood–brain barrier to various sized molecules. Am J Phys. 1985;248:H712–8. https://doi.org/10.1152/ajpheart.1985.248.5.H712.
3. On NH, Miller DW. Transporter-based delivery of anticancer drugs to the brain: improving brain penetration by minimizing drug efflux at the blood–brain barrier. Curr Pharm Des. 2014;20:1499–509.
4. Oldendorf WH. Lipid solubility and drug penetration of the blood brain barrier. Proc Soc Exp Biol Med. 1974;147:813–5.

5. Boockvar JA, Tsiouris AJ, Hofstetter CP, Kovanlikaya I, Fralin S, Kesavabhotla K, et al. Safety and maximum tolerated dose of superselective intraarterial cerebral infusion of bevacizumab after osmotic blood–brain barrier disruption for recurrent malignant glioma. Clinical article. J Neurosurg. 2011;114:624–32. https://doi.org/10.3171/2010.9.JNS101223.
6. Lesniak WG, Chu C, Jablonska A, Du Y, Pomper MG, Walczak P, et al. A distinct advantage to intraarterial delivery of 89zr-bevacizumab in pet imaging of mice with and without osmotic opening of the blood–brain barrier. J Nucl Med. 2019;60(5):617–22. https://doi.org/10.2967/jnumed.118.218792.
7. Banks WA. Characteristics of compounds that cross the blood–brain barrier. BMC Neurol. 2009;9(Suppl 1):S3. https://doi.org/10.1186/1471-2377-9-S1-S3.
8. Janowski M, Walczak P, Pearl MS. Predicting and optimizing the territory of blood–brain barrier opening by superselective intra-arterial cerebral infusion under dynamic susceptibility contrast MRI guidance. J Cereb Blood Flow Metab. 2016;36:569–75. https://doi.org/10.1177/0271678X15615875.
9. Lyczek A, Arnold A, Zhang J, Campanelli JT, Janowski M, Bulte JW, et al. Transplanted human glial-restricted progenitors can rescue the survival of dysmyelinated mice independent of the production of mature, compact myelin. Exp Neurol. 2017;291:74–86. https://doi.org/10.1016/j.expneurol.2017.02.005.
10. Zawadzki M, Walecki J, Kostkiewicz B, Kostyra K, Pearl MS, Solaiyappan M, et al. Real-time MRI guidance for intra-arterial drug delivery in a patient with a brain tumor: technical note. BMJ Case Rep. 2019;12:pii: e014469. https://doi.org/10.1136/bcr-2018-014469.
11. Ingram JR, Schmidt FI, Ploegh HL. Exploiting Nanobodies' singular traits. Annu Rev Immunol. 2018;36:695–715. https://doi.org/10.1146/annurev-immunol-042617-053327.
12. Bannas P, Lenz A, Kunick V, Well L, Fumey W, Rissiek B, et al. Molecular imaging of tumors with nanobodies and antibodies: timing and dosage are crucial factors for improved in vivo detection. Contrast Media Mol Imaging. 2015;10:367–78. https://doi.org/10.1002/cmmi.1637.
13. Kannan RM, Nance E, Kannan S, Tomalia DA. Emerging concepts in dendrimer-based nanomedicine: from design principles to clinical applications. J Intern Med. 2014;276:579–617. https://doi.org/10.1111/joim.12280.
14. Chauhan AS. Dendrimers for Drug Delivery. Molecules. 2018;23:938. https://doi.org/10.3390/molecules23040938.
15. Kannan S, Dai H, Navath RS, Balakrishnan B, Jyoti A, Janisse J, et al. Dendrimer-based postnatal therapy for neuroinflammation and cerebral palsy in a rabbit model. Sci Transl Med. 2012;4:130ra46. https://doi.org/10.1126/scitranslmed.3003162.
16. Balakrishnan B, Nance E, Johnston MV, Kannan R, Kannan S. Nanomedicine in cerebral palsy. Int J Nanomedicine. 2013;8:4183–95. https://doi.org/10.2147/IJN.S35979.
17. Zhang F, Mastorakos P, Mishra MK, Mangraviti A, Hwang L, Zhou J, et al. Uniform brain tumor distribution and tumor associated macrophage targeting of systemically administered dendrimers. Biomaterials. 2015;52:507–16. https://doi.org/10.1016/j.biomaterials.2015.02.053.
18. Qiu J, Kong L, Cao X, Li A, Wei P, Wang L, et al. Enhanced delivery of therapeutic siRNA into glioblastoma cells using dendrimer-entrapped gold nanoparticles conjugated with beta-cyclodextrin. Nanomaterials. 2018;8:131. https://doi.org/10.3390/nano8030131.
19. Van den Abbeele A, De Clercq S, De Ganck A, De Corte V, Van Loo B, Soror SH, et al. A llama-derived gelsolin single-domain antibody blocks gelsolin-G-actin interaction. Cell Mol Life Sci. 2010;67:1519–35. https://doi.org/10.1007/s00018-010-0266-1.
20. Vosjan MJ, Perk LR, Visser GW, Budde M, Jurek P, Kiefer GE, et al. Conjugation and radiolabeling of monoclonal antibodies with zirconium-89 for PET imaging using the bifunctional chelate p-isothiocyanatobenzyl-desferrioxamine. Nat Protoc. 2010;5:739–43. https://doi.org/10.1038/nprot.2010.13.
21. Chu C, Liu G, Janowski M, Bulte JWM, Li S, Pearl M, et al. Real-time MRI guidance for reproducible hyperosmolar opening of the blood–brain barrier in mice. Front Neurol. 2018;9:921. https://doi.org/10.3389/fneur.2018.00921.
22. Tellinghuisen J. Least squares with non-normal data: estimating experimental variance functions. Analyst. 2008;133:161–6. https://doi.org/10.1039/b708709h.
23. Laznickova A, Biricova V, Laznicek M, Hermann P. Mono(pyridine-N-oxide) DOTA analog and its G1/G4-PAMAM dendrimer conjugates labeled with 177Lu: radiolabeling and biodistribution studies. Appl Radiat Isot. 2014;84:70–7. https://doi.org/10.1016/j.apradiso.2013.10.021.
24. Sadekar S, Ray A, Janat-Amsbury M, Peterson CM, Ghandehari H. Comparative biodistribution of PAMAM dendrimers and HPMA copolymers in ovarian-tumor-bearing mice. Biomacromolecules. 2011;12:88–96. https://doi.org/10.1021/bm101046d.
25. Zhang Y, Sun Y, Xu X, Zhang X, Zhu H, Huang L, et al. Synthesis, biodistribution, and microsingle photon emission computed tomography (SPECT) imaging study of technetium-99m labeled PEGylated dendrimer poly(amidoamine) (PAMAM)-folic acid conjugates. J Med Chem. 2010;53:3262–72. https://doi.org/10.1021/jm901910j.
26. Lesniak WG, Mishra MK, Jyoti A, Balakrishnan B, Zhang F, Nance E, et al. Biodistribution of fluorescently labeled PAMAM dendrimers in neonatal rabbits: effect of neuroinflammation. Mol Pharm. 2013;10:4560–71. https://doi.org/10.1021/mp400371r.
27. Boswell CA, Sun X, Niu W, Weisman GR, Wong EH, Rheingold AL, et al. Comparative in vivo stability of copper-64-labeled cross-bridged and conventional tetraazamacrocyclic complexes. J Med Chem. 2004;47:1465–74. https://doi.org/10.1021/jm030383m.
28. Gomes JR, Cabrito I, Soares HR, Costelha S, Teixeira A, Wittelsberger A, et al. Delivery of an anti-transthyretin Nanobody to the brain through intranasal administration reveals transthyretin expression and secretion by motor neurons. J Neurochem. 2018;145:393–408. https://doi.org/10.1111/jnc.14332.
29. Samec N, Jovcevska I, Stojan J, Zottel A, Liovic M, Myers MP, et al. Glioblastoma-specific anti-TUFM nanobody for in-vitro immunoimaging and cancer stem cell targeting. Oncotarget. 2018;9:17282–99. https://doi.org/10.18632/oncotarget.24629.
30. McMurphy T, Xiao R, Magee D, Slater A, Zabeau L, Tavernier J, et al. The anti-tumor activity of a neutralizing nanobody targeting leptin receptor in a mouse model of melanoma. PLoS One. 2014;9:e89895. https://doi.org/10.1371/journal.pone.0089895.
31. Vaidyanathan G, McDougald D, Choi J, Koumarianou E, Weitzel D, Osada T, et al. Preclinical evaluation of 18F-labeled anti-HER2 Nanobody conjugates for imaging HER2 receptor expression by Immuno-PET. J Nucl Med. 2016;57:967–73. https://doi.org/10.2967/jnumed.115.171306.
32. Bala G, Blykers A, Xavier C, Descamps B, Broisat A, Ghezzi C, et al. Targeting of vascular cell adhesion molecule-1 by 18F-labelled nanobodies for PET/CT imaging of inflamed atherosclerotic plaques. Eur Heart J Cardiovasc Imaging. 2016;17:1001–8. https://doi.org/10.1093/ehjci/jev346.